



Cite this: *RSC Adv.*, 2019, 9, 626

## Photo-enhanced gas sensing of SnS<sub>2</sub> with nanoscale defects†

Wen-Jie Yan,<sup>a</sup> Deng-Yun Chen,<sup>a</sup> Huei-Ru Fuh,<sup>\*bc</sup> Ying-Lan Li,<sup>a</sup> Duan Zhang,<sup>a</sup> Huajun Liu,<sup>d</sup> Gang Wu,<sup>a</sup> Lei Zhang,<sup>e</sup> Xiangkui Ren,<sup>e</sup> Jiung Cho,<sup>f</sup> Miri Choi,<sup>g</sup> Byong Sun Chun,<sup>h</sup> Cormac Ó. Coileáin,<sup>a</sup> Hong-Jun Xu,<sup>a</sup> Zhi Wang,<sup>a</sup> Zhaotan Jiang,<sup>a</sup> Ching-Ray Chang<sup>\*b</sup> and Han-Chun Wu<sup>id</sup><sup>\*a</sup>

Recently a SnS<sub>2</sub> based NO<sub>2</sub> gas sensor with a 30 ppb detection limit was demonstrated but this required high operation temperatures. Concurrently, SnS<sub>2</sub> grown by chemical vapor deposition is known to naturally contain nanoscale defects, which could be exploited. Here, we significantly enhance the performance of a NO<sub>2</sub> gas sensor based on SnS<sub>2</sub> with nanoscale defects by photon illumination, and a detection limit of 2.5 ppb is achieved at room temperature. Using a classical Langmuir model and density functional theory simulations, we show S vacancies work as additional adsorption sites with fast adsorption times, higher adsorption energies, and an order of magnitude higher resistance change compared with pristine SnS<sub>2</sub>. More interestingly, when electron–hole pairs are excited by photon illumination, the average adsorption time first increases and then decreases with NO<sub>2</sub> concentration, while the average desorption time always decreases with NO<sub>2</sub> concentration. Our results give a deep understanding of photo-enhanced gas sensing of SnS<sub>2</sub> with nanoscale defects, and thus open an interesting window for the design of high performance gas sensing devices based on 2D materials.

Received 25th October 2018  
 Accepted 20th December 2018

DOI: 10.1039/c8ra08857h

rsc.li/rsc-advances

Nitrogen dioxide (NO<sub>2</sub>) is one of the most common hazardous gas pollutants produced as a by-product of industry.<sup>1–4</sup> Notably, NO<sub>2</sub> is also a product yielded from the thermal decomposition of organic nitrates, such as TNT, which is a useful fingerprint for controlling these substances and combating international terrorism.<sup>5</sup> An issue of global concern, serious respiratory diseases can be caused by chronic environmental exposure to as little as 53 ppb NO<sub>2</sub>.<sup>1,4,6</sup> Therefore, the research and development of gas sensors with high sensitivities is always of high priority.<sup>2,7–19</sup> Recently, 2D materials have been used for gas sensing owing to their large surface-to-volume ratios.<sup>13,20</sup> A wide variety of 2D materials, such as graphene,<sup>9,10,14</sup> black

phosphorus,<sup>2,21</sup> metal dichalcogenides,<sup>4,12,15,18,19,22–24</sup> have been studied as high performance gas sensors.<sup>16,20,23,25,26</sup>

As a member of the wide class 2D materials, tin disulfide (SnS<sub>2</sub>) displays many intriguing properties in electronics,<sup>27</sup> photonics and optoelectronics,<sup>27–30</sup> as well as gas monitoring.<sup>24,31–42</sup> It was reported recently by Kalantar-zadeh *et al.* that a SnS<sub>2</sub>-based NO<sub>2</sub> gas sensor with a sensitivity of 0.5 ppm could be improved to 30 ppb when heated to 120 °C.<sup>24</sup> However, an elevated operating temperature typically increases power consumption and thus a more intricate setup is required.<sup>3,10,16,20,24,25,43</sup> Furthermore, the high operating temperature might pose the risk of ignition when detecting in flammable or explosive atmospheres which would limit sensor's application.<sup>44–46</sup> Concurrently, it is known that 2D materials produced by chemical vapor deposition (CVD) usually contain nanoscale defects, such as vacancies, grain boundaries, *etc.* and in particular CVD grown SnS<sub>2</sub> is reported to naturally contain S vacancies.<sup>47</sup> It is well known that nanoscale defects can significantly affect gas sensing performance.<sup>48</sup> Thus it is important to investigate how S vacancies in SnS<sub>2</sub> affect the gas sensing performance. Furthermore, it should be also noted that compared with thermally assisted gas sensing, a photon assisted arrangement can not only improve the detection limit of gas sensor but also can accelerate the desorption ratio.<sup>15,19,49–51</sup> It is reported that SnS<sub>2</sub> nanosheets exhibit excellent optoelectronics properties,<sup>27–30</sup> making it feasible to improve the gas sensing performance of SnS<sub>2</sub> with photon illumination.

<sup>a</sup>School of Physics, Beijing Institute of Technology, Beijing 100081, P. R. China. E-mail: wuhc@bit.edu.cn

<sup>b</sup>Department of Physics, National Taiwan University, Taipei 106, Taiwan. E-mail: crchang@phys.ntu.edu.tw

<sup>c</sup>Department of Chemical Engineering & Materials Science, Yuan Ze University, Taoyuan City 320, Taiwan. E-mail: hrufuh@saturn.yzu.edu.tw

<sup>d</sup>Institute of Plasma Physics, Chinese Academy of Sciences, Hefei 230031, P. R. China

<sup>e</sup>School of Chemical Engineering and Technology, Tianjin University, Tianjin 300072, P. R. China

<sup>f</sup>Western Seoul Center, Korea Basic Science Institute, Seoul 03579, Republic of Korea

<sup>g</sup>Chuncheon Center, Korea Basic Science Institute, Chuncheon 24341, Republic of Korea

<sup>h</sup>Division of Industrial Metrology, Korea Research Institute of Standards and Science, Daejeon 305-340, Republic of Korea

† Electronic supplementary information (ESI) available. See DOI: 10.1039/c8ra08857h



In this work, we demonstrate that photon illumination can significantly enhance the performance of NO<sub>2</sub> gas sensors based on SnS<sub>2</sub>, and an ultra-low concentration sensitivity of 2.5 ppb is achieved at room temperature. The results also show that gas sensitivity increases linearly with decreasing SnS<sub>2</sub> nanosheet thickness. In combination with a classical Langmuir model and density functional theory simulations, we show that S vacancies work as additional adsorption sites with fast adsorption times, higher adsorption energies, and greater resistance change compared with pristine SnS<sub>2</sub>. Moreover, when electron-hole pairs are excited by photon illumination, the average adsorption time first increases and then decreases with NO<sub>2</sub> concentration. Considering safety, energy efficiency and sensitivity, SnS<sub>2</sub>-based photo-illuminated gas sensors provide a possible way to realize the measurement of ultra-low concentrations of NO<sub>2</sub>, or other hazardous gases, for environmental, industrial and domestic monitoring.

Fig. 1(a) shows a schematic of the chemical vapor deposition (CVD) arrangement for the SnS<sub>2</sub> nanosheet growth. A sulfur powder source was placed upstream in the furnace. Sn granules were smashed into pieces and were placed at the center of the furnace. Several pieces of a diced 300 nm SiO<sub>2</sub>/Si (1 cm × 1 cm) wafer were placed downstream as substrates for SnS<sub>2</sub> growth. Further details of the SnS<sub>2</sub> growth can be found in the Experimental section. After the reaction, SnS<sub>2</sub> nanosheets were formed on the SiO<sub>2</sub>/Si substrates. Fig. 1(b) shows a scanning electron microscopy (SEM) image of a SnS<sub>2</sub> flake grown on a SiO<sub>2</sub>/Si substrate. The flakes typically have a semi-hexagonal structure with lateral dimensions ranging from 10 μm to 228 μm (Fig. S1†). Fig. 1(c) gives the structure of SnS<sub>2</sub> with the purple and yellow spheres representing Sn and S atoms, respectively.

Atomic force microscopy (AFM) was used to determine the thicknesses of the nanosheets. Fig. 2(a) shows the height profile of an ultrathin SnS<sub>2</sub> nanosheet with a thickness ≈ 6 nm (≈ 10 layers, 0.6 nm per layer),<sup>30</sup> as measured along the red dotted line in the inset image, (more examples in Fig. S2†). The SnS<sub>2</sub> was also characterized by Raman spectroscopy, as shown in

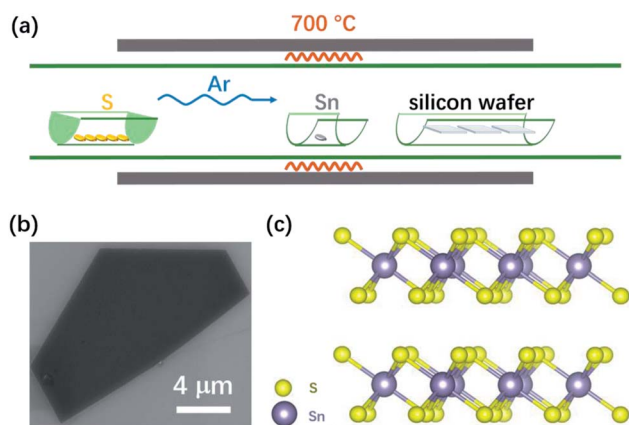


Fig. 1 (a) A schematic of CVD growth setup. (b) A SEM image of a semi-hexagonal nanosheet of SnS<sub>2</sub>. (c) Schematic of SnS<sub>2</sub> structure with purple and yellow spheres representing Sn and S atoms, respectively.

Fig. 2(b). Only a single Raman peak (A<sub>1g</sub> mode at 314 cm<sup>-1</sup>) can be clearly observed for an 8 nm thick SnS<sub>2</sub> nanosheet, and an additional Raman peak, the E<sub>g</sub> mode at 205 cm<sup>-1</sup>, appears for a thicker 60 nm SnS<sub>2</sub> nanosheet, which is consistent with literature.<sup>28,52</sup> The E<sub>g</sub> mode is due to the scattering centers for in-plane scattering. When the thickness drops below 8 nm the intensity decreases and effectively becomes undetectable.<sup>30</sup> The crystal structure of few-layer SnS<sub>2</sub> was further characterized by high-resolution transmission electronic microscopy (HRTEM), indicating the single-crystalline structure of the SnS<sub>2</sub> (Fig. 2(c)). The measured width of the lattice fringes is ≈ 0.32 nm which corresponds to the (100) plane of SnS<sub>2</sub>. Fig. 2(d) shows the selected-area-electron-diffraction (SAED) pattern, which displays six-fold symmetry diffraction spots, confirming the hexagonal single-crystalline nature of the flake. Additionally, Sn and S elemental mapping using Electron Energy Loss Spectroscopy (EELS), in Fig. 2(f), of the selected area shown in Fig. 2(e), indicates the atomic ratio of Sn : S ≈ 1 : 1.86, suggesting the presence of S vacancies in the SnS<sub>2</sub>, which is consistent with earlier reports.<sup>47</sup>

Before studying the photo-enhanced gas sensing properties of SnS<sub>2</sub>, we first explored its optoelectronic properties. Fig. 3(a) is an optical image of a typical device prepared from a semi-hexagonal SnS<sub>2</sub> nanosheet on a SiO<sub>2</sub>/Si substrate with 300 nm thick SiO<sub>2</sub>. Fig. 3(b) shows the current *versus* voltage I<sub>DS</sub>-V<sub>DS</sub> (DS, Drain-Source) characteristics of the device with the gate voltage (V<sub>G</sub>) varied from -20 V to 20 V in steps of 5 V and Fig. 3(c) plots the relationship between I<sub>DS</sub> and V<sub>G</sub>, with V<sub>DS</sub> ranging from -10 V to +10 V in steps of 2.5 V indicating transfer characteristics of the device. From Fig. 3(b and c) it is apparent that our CVD grown SnS<sub>2</sub> nanosheets are n-type and the mobility is around 9.7 cm<sup>2</sup> V<sup>-1</sup> s<sup>-1</sup> which further supports the presence of the S vacancies.<sup>47</sup> Fig. 3(d and e) shows the I-V characteristics of the device at V<sub>G</sub> = 0 V in the dark and under illumination by 532 nm and 650 nm lasers, in ambient conditions. It is found there is a notable change in the I<sub>DS</sub> response going from dark to illuminated, and the enhancement of I<sub>DS</sub> for the 532 nm laser is relatively larger than that observed for the 650 nm laser. Fig. 3(f) further shows the time resolved photo response of another device at V<sub>DS</sub> = 5 V, where the light intensity of the 532 nm laser was 3.0 mW cm<sup>-2</sup>. The responsivity (R<sub>i</sub>) and external quantum efficiency (EQE) are calculated to be 31 A W<sup>-1</sup> and 7.7 × 10<sup>3</sup>%, respectively (details of this calculation can be found in ESI Formula (2)†).

Fig. 4(a) is an optical image of a typical SnS<sub>2</sub>-based gas sensor fabricated by conventional UV-lithography. The distance between each of the contacts is approximately 5 μm. Fig. 4(b and c) show the dynamic-sensing responses without and with 405 nm laser irradiation, respectively, where the NO<sub>2</sub> gas concentration was varied from 6.5 ppb to 130 ppb. The sensor response is defined as  $\Delta R/R_0 = (R_{\text{NO}_2} - R_{\text{N}_2})/R_{\text{N}_2}$ , where R<sub>N<sub>2</sub></sub> and R<sub>NO<sub>2</sub></sub> are the resistances of the device when exposed to pure N<sub>2</sub> and a NO<sub>2</sub> gas mix, respectively. In the dark environment, the sensor has the first observable response at 78 ppb NO<sub>2</sub>. Remarkably, by illuminating the sensor with a 405 nm laser a clear response is observed at 13 ppb NO<sub>2</sub>. To confirm this, Fig. 4(d) plotted I<sub>DS</sub>-V<sub>DS</sub> curves of the same device under



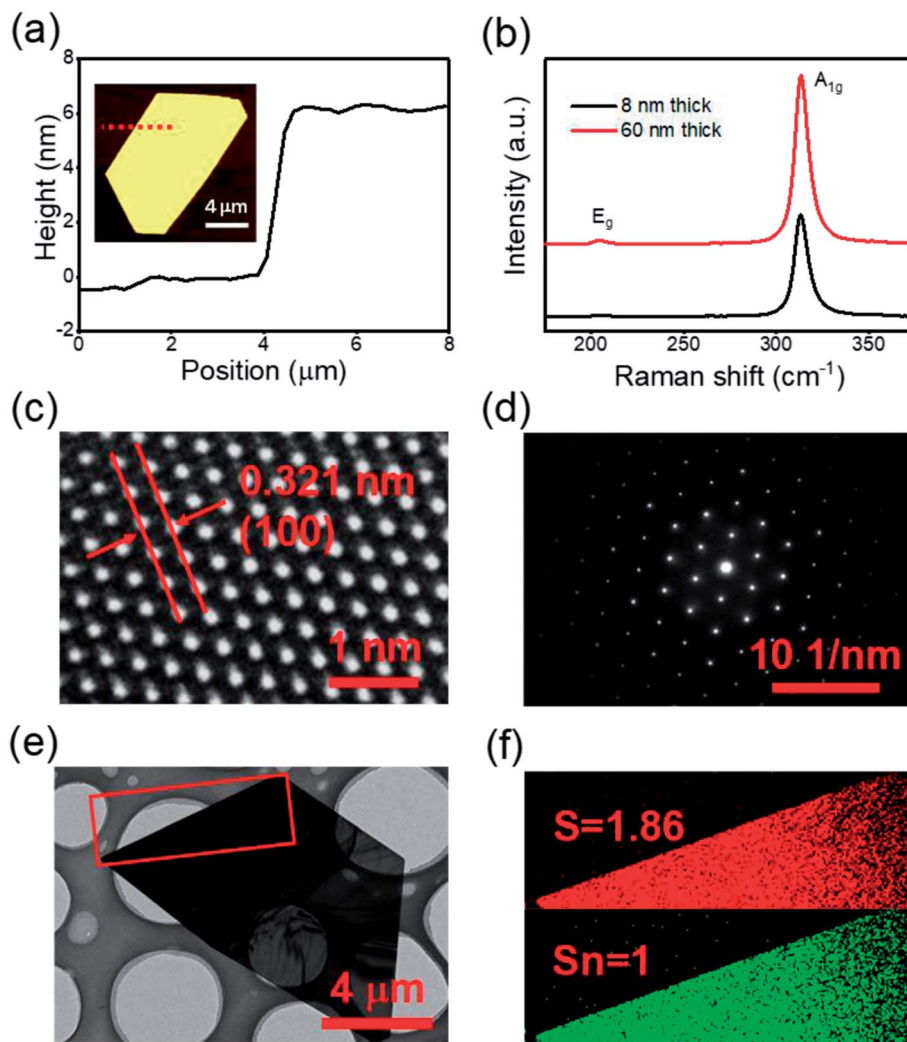


Fig. 2 Characterization of CVD produced single crystal  $\text{SnS}_2$  nanosheet. (a) Height profiles of the dashed line shown in the inset AFM image. (b) Raman spectra of  $\text{SnS}_2$  nanosheet. (c) High-resolution TEM image and corresponding (d) selected-area-electron-diffraction (SAED) pattern of a typical grown  $\text{SnS}_2$  flake. (e) Low magnification bright field TEM image of a semi-hexagonal  $\text{SnS}_2$  nanosheet. (f) EELS elemental mapping of the selected area in (e) with the result  $\text{Sn} : \text{S} = 1 : 1.86$ .

different  $\text{NO}_2$  concentrations. It is apparent that in the dark environment, the  $I_{\text{DS}}-V_{\text{DS}}$  curves for 0 ppb, 26 ppb and 52 ppb  $\text{NO}_2$  merge together. In contrast with this, clear distinctions can be observed between 0 ppb, 26 ppb and 52 ppb  $\text{NO}_2$  with 405 nm laser illumination. A similar effect was observed with 650 nm (26 ppb) and 785 nm (52 ppb) lasers (Fig. S3†). Thus, laser illumination can improve the gas sensing capabilities of such devices.

The stability of a sensor is critical for practical applications. Multi-cycle dynamic sensing responses of the  $\text{SnS}_2$ -based sensor against to 13, 39 and 78 ppb  $\text{NO}_2$  are used here to demonstrate the good repeatability and reproducibility of such  $\text{SnS}_2$ -based sensors (Fig. 4(e)). Moreover, the response to varied concentrations of  $\text{NO}_2$  with a relative humidity 64% is also showed in Fig. S5(d)†. These indicate the reliability of the illuminated  $\text{SnS}_2$ -based sensor and that the presence of water does not degrade performance.

To probe the function of sensitivity *versus* the thickness of  $\text{SnS}_2$ , we also tested more than 10 samples with different

thicknesses, ranging from 17 nm to 370 nm (Fig. S4–S9†). It is found that the sensitivity increases linearly as the thickness of the  $\text{SnS}_2$ -nanosheets is reduced, as shown in Fig. 4(f). Remarkably, a significant response is unmistakably observed at 2.5 ppb  $\text{NO}_2$  for a 22 nm thick  $\text{SnS}_2$  based gas sensor (Fig. S8(d)†), suggesting that  $\text{SnS}_2$  based gas sensor can achieve a  $\text{NO}_2$  detection limit better than 2.5 ppb. To the best of our knowledge, this is the lowest detection limit for  $\text{NO}_2$  achieved using  $\text{SnS}_2$  devices to date, which is an improvement by a factor greater than ten on previous work.<sup>24</sup> Table 1 summarizes and compares the important features of  $\text{SnS}_2$ -based  $\text{NO}_2$  gas sensors from literature. Kalantar-zadeh *et al.* heated their  $\text{SnS}_2$  flake sensor to 120 °C to achieve a 30 ppb detection limit.<sup>24</sup> Hao *et al.* heated a  $\text{SnS}_2$  flower interspersed with  $\text{SnO}_2$  to 100 °C to reach a 125 ppb detection limit.<sup>31</sup> Ahn *et al.* built utilized vertical  $\text{SnS}_2$  flake structures to detect  $\text{NO}_2$  at 300 ppb, probably under its optimum conditions at 160 °C.<sup>39</sup> Li *et al.* heated  $\text{SnS}_2$  their flake devices to 120 °C to attain a 600 ppb detection limit.<sup>40</sup> Wang *et al.* heated a  $\text{SnS}_2$ - $\text{SnO}_2$  composite flake device to 80 °C for



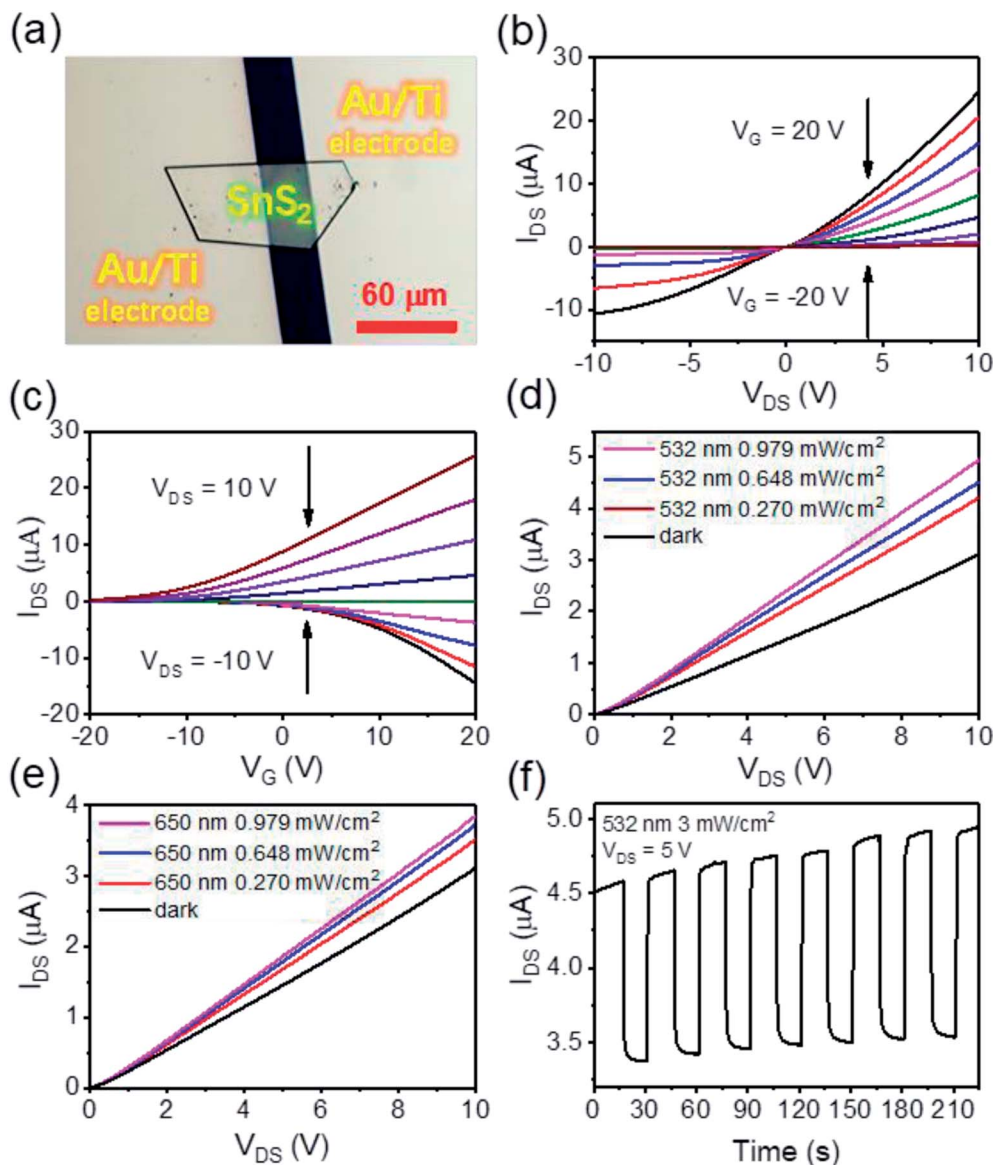


**Fig. 3** (a) Optical microscope image of a SnS<sub>2</sub> device for the following measurement. (b)  $I_{DS}$ - $V_{DS}$  curves for different  $V_G$  from -20 to 20 V in steps of 5 V. (c)  $I_{DS}$ - $V_G$  curves for different  $V_{DS}$  from -10 to 10 V in steps of 2.5 V. (d)  $I_{DS}$ - $V_{DS}$  curves of device under 532 nm laser illumination by different energy densities. (e)  $I_{DS}$ - $V_{DS}$  curves of device under 650 nm laser illumination by different energy densities. (f) Time-resolved photon response of another SnS<sub>2</sub> device measured in vacuum ( $V_{DS} = 5$  V, 532 nm laser 0.979 mW cm<sup>-2</sup>).

a 1000 ppb detection limit.<sup>41</sup> While Xue *et al.* used SnS<sub>1.5</sub>/Se<sub>0.5</sub> flake devices to detect 1000 ppb NO<sub>2</sub> at room temperature.<sup>42</sup>

To better illustrate the photo-enhanced gas sensing properties, we summarized the signal/noise (S/N) ratios of the  $\Delta R/R_0$  from response in Fig. 4(b and c) into Fig. 5(a).<sup>53-57</sup> It is clear that there are 3 distinct regions. At high concentrations of NO<sub>2</sub> the S/N is almost constant (dark and 785 nm). This means the surface adsorption is almost saturated and has reached its upper limit. Increasing gas concentration does not increase the signal. In the medium concentration range (classic region), S/N increases linearly with gas concentration. In the low NO<sub>2</sub> concentration regime (<52 ppb) no effective signal is detected for dark conditions. But a signal is detected with illumination, which is especially prominent for the short wavelength light, indicating extra energy is required to desorb NO<sub>2</sub> from surface of SnS<sub>2</sub>.

We fitted the desorption (adsorption) sections of the dynamic-sensing response curves under different laser illuminations with the expression  $y = y_0 + Ae^{-\frac{x}{\tau_D}}$  ( $y = y_0 + Ae^{\frac{x}{\tau_A}}$ ), where  $\tau_D$  ( $\tau_A$ ) is the average desorption (adsorption) time. The average desorption times and average adsorption times under various laser illuminations are summarized in Fig. 5(b) and (c) respectively. It is clear illumination not only enables ultra-high sensitivity but also results in faster desorption and better S/N ratios. Interestingly, with the 405 nm laser illumination, the adsorption time first increases and then decreases with gas concentration when the concentration reaches ~78 ppb. While for dark and 785 nm laser illumination, both the desorption and adsorption times decrease with increasing gas concentration.



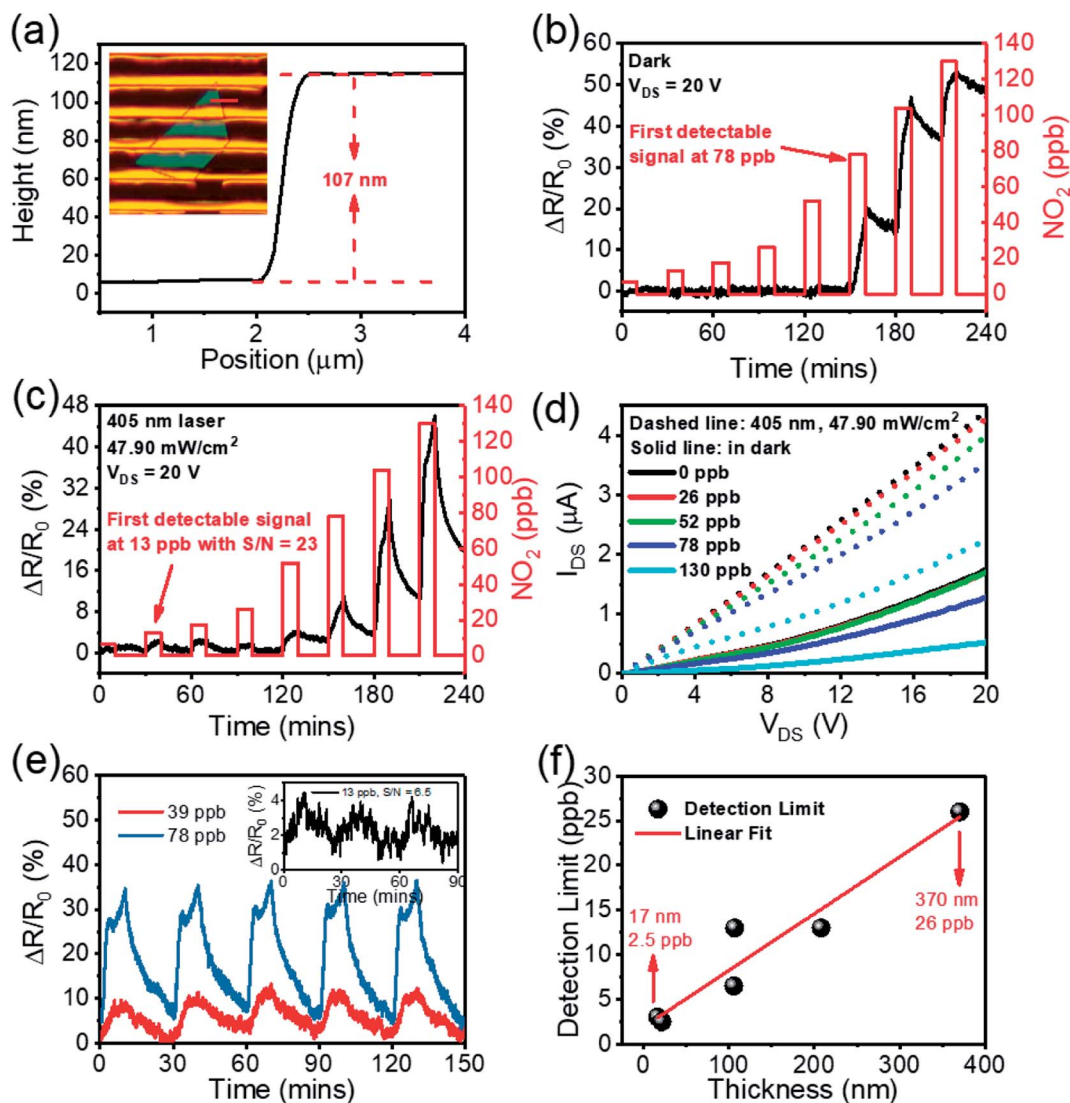


Fig. 4 (a) Optical microscope image of a SnS<sub>2</sub> device for gas sensor measurements. Dynamic sensing response of  $\Delta R/R_0$  change versus time for the SnS<sub>2</sub>-based sensor upon exposure to NO<sub>2</sub> gas with concentrations ranging from 6.5 ppb to 130 ppb under (b) dark environment and (c) 405 nm laser irradiation. (d) Comparison  $I_{DS}$ – $V_{DS}$  curves of the device under different light illuminations and NO<sub>2</sub> concentrations. (e) Multi-cycle responses of sensor when exposed to concentrations of 13, 39, and 78 ppb NO<sub>2</sub>. (f) Sensitivity as a function of SnS<sub>2</sub> thickness.

We replotted the dynamic-sensing response curves under 405 nm laser illumination based on the Langmuir model (Fig. 6).<sup>58</sup> There are two classes of adsorption sites. Similar behavior has been observed under 785 nm and 650 nm laser illumination (Fig. S10†). For the adsorption process, NO<sub>2</sub> can

adsorb on both sites but prefer sites with fast adsorption times. With increasing gas concentration, more NO<sub>2</sub> molecules will be adsorbed on sites with slower adsorption times which increases the average adsorption time. At yet higher gas concentrations all the fast adsorption time sites will be occupied. The NO<sub>2</sub>

Table 1 Comparison of NO<sub>2</sub> gas sensors performance for SnS<sub>2</sub>-based sensors. Our SnS<sub>2</sub> gas sensor achieves a remarkably detection limit more than 10 times better than values reported in previous works

No.	Material	Limit of detection	Special method	Reference
1	SnS <sub>2</sub> flake	2.5 ppb	UV illumination	This work
2	SnS <sub>2</sub> flake	30 ppb	Heater	24
3	SnS <sub>2</sub> /SnO <sub>2</sub> flakes	125 ppb	Heater	31
4	SnS <sub>2</sub> flakes	300 ppb	Heater	39
5	SnS <sub>2</sub> flakes	600 ppb	Heater	40
6	SnS <sub>2</sub> /SnO <sub>2</sub>	1000 ppb	Heater	41
7	SnS <sub>1.5</sub> /Se <sub>0.5</sub>	1000 ppb	Room temperature	42



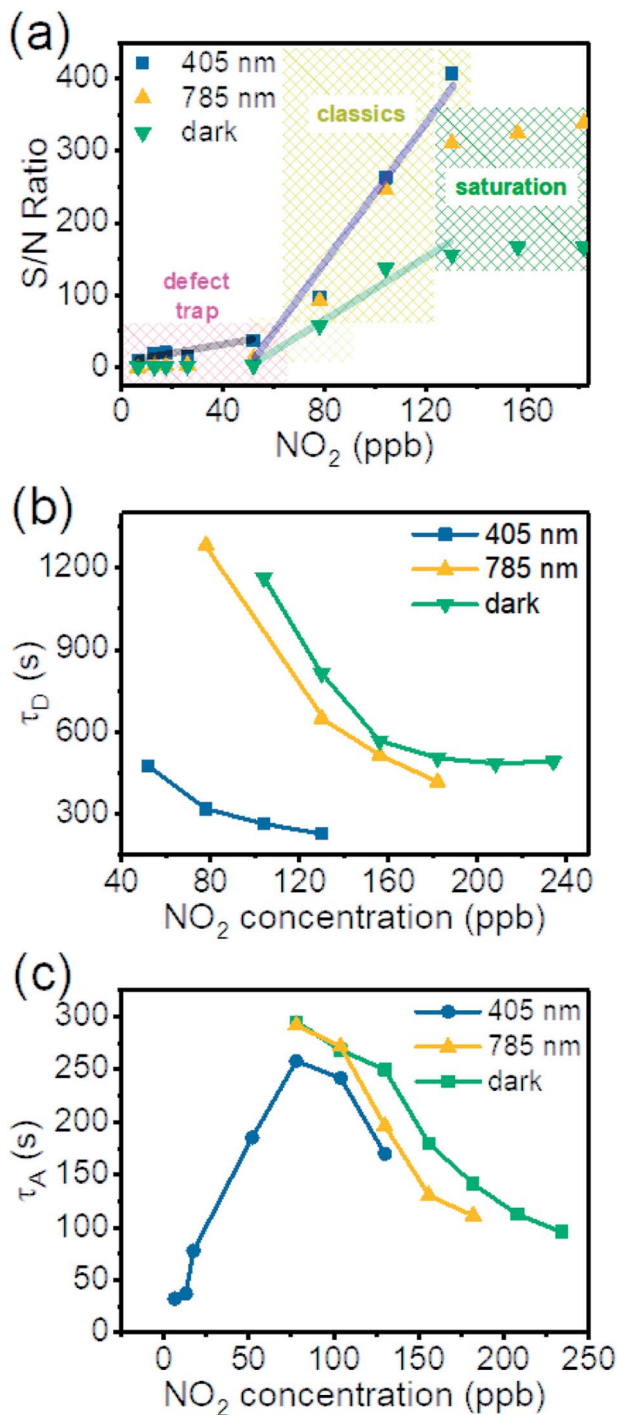


Fig. 5 (a) Comparison of S/N ratio of the dynamic response of the SnS<sub>2</sub> sensor for dark and illuminated environments. Green line is a linear fitting of dark environment data between 52 to 130 ppb NO<sub>2</sub>. Black line and blue line are linear fitting of 405 nm illumination data between 6.5 to 52 ppb and 52 to 130 ppb NO<sub>2</sub>. (b) Desorption time as a function of gas concentration. (c) Adsorption time as a function of gas concentration.

molecules will be adsorbed on the sites with slow adsorption times, which can be treated as one site adsorption. According to the Langmuir model considering one adsorption site,  $\tau_D = \frac{1}{aN_c}$ , where  $N_c$  is proportional to the gas concentration.

This is why the average adsorption time first increases and then decreases with gas concentration. On the other hand, for the desorption process at low concentrations it is the sites with slow desorption times that are the limiting factor. With increasing gas concentration, more molecules will be desorbed from the sites with faster desorption times, thus decreasing the average desorption time. Moreover, NO<sub>2</sub> molecules adsorb on sites with faster adsorption times will significantly decrease the overall conductance compared with NO<sub>2</sub> molecules bound to sites with slow adsorption.

To investigate whether S vacancies could give such an effect, we calculated the adsorption energy, charge density distribution, and conductance of NO<sub>2</sub> molecules on a SnS<sub>2</sub> monolayer with and without S vacancies. Details of the calculations can be found in the Methods section. Fig. 7(a) and (b) show the optimized atomic structures of a NO<sub>2</sub> molecule adsorbed on pristine SnS<sub>2</sub> and SnS<sub>2</sub> with a surface S vacancy respectively. For a NO<sub>2</sub> molecule adsorbed on pristine SnS<sub>2</sub>, the perpendicular distance between the O atom of a NO<sub>2</sub> molecule and the nearest S atom of the SnS<sub>2</sub> ( $R$ ) is about 2.95 Å and it is decreased significantly to 0.5 Å for a NO<sub>2</sub> molecule on SnS<sub>2</sub> with a S vacancy, indicating the S vacancy induces strong adsorption between SnS<sub>2</sub> and NO<sub>2</sub>. To understand the adsorption mechanism, the adsorption energy as a function of distance  $R$  is plotted in Fig. 7(c). The adsorption energy is 1.011 eV when a NO<sub>2</sub> molecule adsorbed on SnS<sub>2</sub> with a S vacancy. While for a NO<sub>2</sub> molecule adsorbed on pristine SnS<sub>2</sub>, the corresponding adsorption energy is only 116 meV. Thus, NO<sub>2</sub> molecules adsorbed on the SnS<sub>2</sub> monolayer with S vacancies have a larger adsorption energy compared with a pristine SnS<sub>2</sub> monolayer, indicating that extra energy is required to desorb NO<sub>2</sub> molecule from the S vacancy site (Fig. 7(d)). The adsorption energy for chemisorption is usually an energy of 1–10 eV, but for physisorption the energy is smaller than this. Therefore, the adsorption mechanism may change from physisorption to chemisorption when a NO<sub>2</sub> molecule adsorbed on SnS<sub>2</sub> with S vacancy. Moreover, there is a large partial charge transfer between S and the O atoms of a NO<sub>2</sub> molecule adsorbed on SnS<sub>2</sub> with S vacancy in Fig. 7(e) and (f).

The electrical conductivity of an NO<sub>2</sub> molecule adsorbed on pristine SnS<sub>2</sub> and on SnS<sub>2</sub> with a single S vacancy at 300 K are shown in Fig. 8. We found that monolayer SnS<sub>2</sub> contains a narrow electrical conductivity tail near  $\mu = 0$  resulting from electrons crossing the Fermi level from thermal agitation at  $T = 300$  K, shown in Fig. 8(a). When this pristine SnS<sub>2</sub> adsorbs an NO<sub>2</sub> molecule there is an additional conductivity peak region near  $\mu = 0$  with small values of  $1.1 \times 10^3$  and  $3.0 \times 10^2$  ( $1/\Omega \text{ m}^{-1}$ ) for  $\sigma_{xx}$  and  $\sigma_{yy}$ , respectively, as shown in Fig. 8(b). However for SnS<sub>2</sub> with a S vacancy adsorbing a NO<sub>2</sub> molecule, there is a broad additional conductivity region around  $\mu = 0$  with values about  $1.5 \times 10^4$  and  $1.9 \times 10^4$  ( $1/\Omega \text{ m}^{-1}$ ) for  $\sigma_{xx}$  and  $\sigma_{yy}$ , respectively, shown in Fig. 8(c). These results from transport and DFT analysis are consistent with the experimental conclusions on the resistance changes, and also indicate charge transfer between NO<sub>2</sub> and SnS<sub>2</sub> is critical. It also suggests that the sites with fast adsorption times are S vacancies and the sites with slow adsorption times are the areas of pristine SnS<sub>2</sub>. To



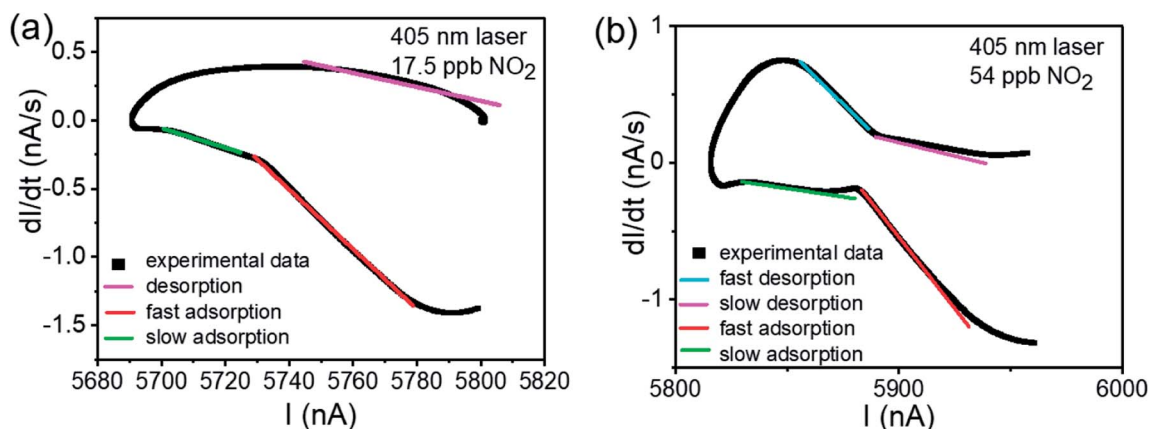


Fig. 6 The  $dI/dt-I$  relationship of Fig. 4(c). (a) The  $dI/dt-I$  curve of 17.5 ppb  $\text{NO}_2$  test. (b) The  $dI/dt-I$  curve of 54 ppb  $\text{NO}_2$  test. In both of two picture, the fitting lines are shown, with blue line depicting the fast desorption process, violet line depicting slow desorption process, red line depicting fast adsorption process and green line depicting slow adsorption process.

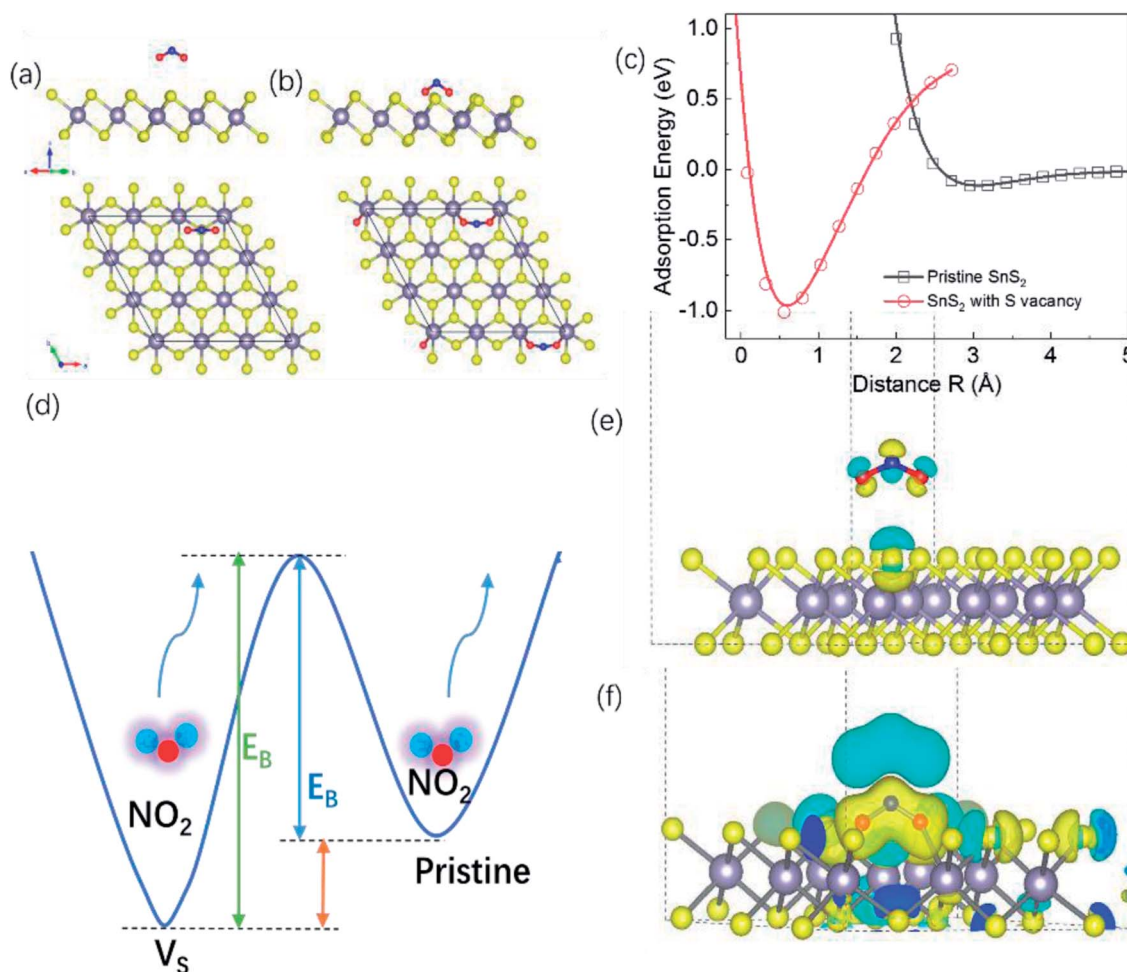


Fig. 7 (a) and (b) Side view and top view of the atomic structure of  $\text{NO}_2$  molecule adsorbed on  $\text{Sn}_9\text{S}_{18}$  and  $\text{Sn}_9\text{S}_{17}$  surfaces, respectively. The large dark spheres represents Sn atoms, while the yellow, blue and red spheres represent the S, N and O atoms, respectively. (c) Adsorption energy as a function of distance  $R$  (defined as the perpendicular distance between the O atom of  $\text{NO}_2$  molecule and the nearest S atom of the  $\text{SnS}_2$ ) for  $\text{NO}_2$  molecule adsorbed on  $\text{Sn}_9\text{S}_{18}$  and  $\text{Sn}_9\text{S}_{17}$  surfaces. (d) Schematic of adsorption energies for an  $\text{NO}_2$  molecule adsorbed on pristine  $\text{SnS}_2$  and on  $\text{SnS}_2$  with a S vacancy. (e) and (f) Charge density difference distribution for  $\text{NO}_2$  molecule adsorbed on  $\text{Sn}_9\text{S}_{18}$  and  $\text{Sn}_9\text{S}_{17}$  surfaces, respectively. The charge density difference in yellow indicate increases in charge density, while blue indicates a decreases in charge density (isosurface =  $0.0015 \text{ eV } \text{\AA}^{-3}$ ).



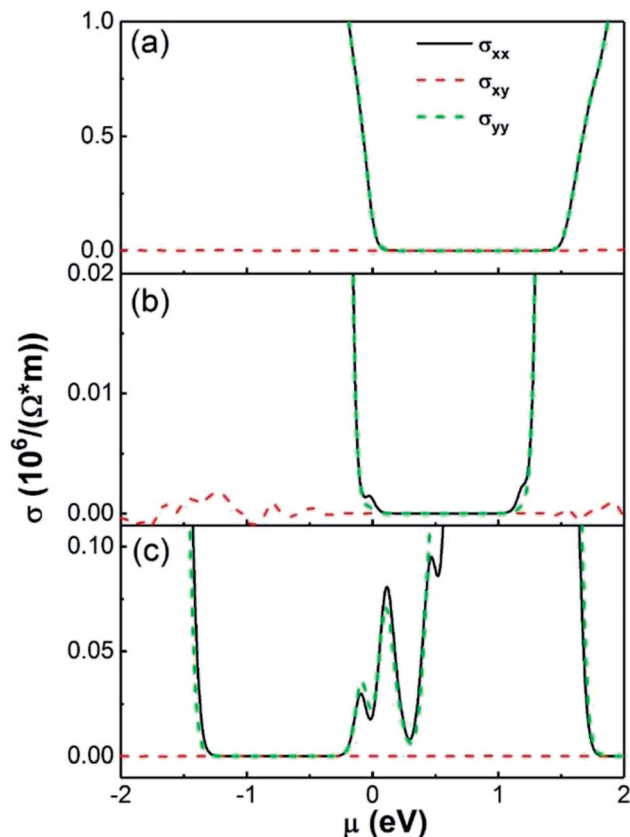


Fig. 8 Electron conductivity of (a) SnS<sub>2</sub> monolayer (b) SnS<sub>2</sub> with adsorbed NO<sub>2</sub> molecule and (c) SnS<sub>2</sub> with S vacancy adsorbed NO<sub>2</sub> molecule which S vacancy concentration is 3.70% at 300 K.

further highlight the importance of S vacancies for the gas sensor performance, we measured the gas performance of gas sensors based on same thick SnS<sub>2</sub> but with different S vacancy density, where the density of S vacancies density was determined by mapping the whole sensor using the EDS equipped in the SEM chamber. A relatively low detection limit or high gas performance was achieved for the sample with higher S vacancies density. For example, for gas sensors based one 106 nm thick SnS<sub>2</sub>, the detection limit for sensor with an atomic ratio of Sn : S ≈ 1 : 1.72 is 6.5 ppb and that for sensor with an atomic ratio of Sn : S ≈ 1 : 1.84 is 13 ppb. We would like to stress that the nanoscale defects are naturally occurring defects forming during chemical vapor deposition. Therefore, they are quite stable when interacting with NO<sub>2</sub> molecules.

It is reported that Schottky junction<sup>59,60</sup> and photo-excited electron-hole pairs can contribute the gas sensing performance. Since our gas sensing performance depends crucially on the wavelength of the photons and same bias voltage is used, here we focus our discussion on effect due to photo-excited electron-hole pairs. We measured the gas sensing performance of another sensor under 365, 405, and 650 nm laser illuminations (Fig. S11†). Only 365 and 405 nm lasers can excite electron-hole pairs, because the band gap of SnS<sub>2</sub> is around 2.2 eV. The 365 and 405 nm laser illuminations have similar detection limit, better than 650 nm. More importantly, the average adsorption time first increases and then decreases with

NO<sub>2</sub> concentration under the 365 and 405 nm laser illuminations, indicating the importance of photo-excited electron-hole pairs for the charge transfer process upon NO<sub>2</sub> adsorption. Therefore, the observed distinct behavior of the adsorption time may be due to the photo-excited electron-hole pairs. We would like to stress that the average adsorption time is faster under the 405 nm photo illumination than the 365 nm, indicating that the 405 nm laser illumination is more efficient since the adsorption spectrum of NO<sub>2</sub> peaks at ~400 nm at 293 K.<sup>61</sup>

In summary, NO<sub>2</sub> gas sensors were fabricated based on CVD grown SnS<sub>2</sub>. An ultra-high sensitivity of 2.5 ppb at room temperature was achieved by utilizing inherent defects under photon illumination. Our results further show S vacancies in SnS<sub>2</sub> work as additional adsorption sites and the detection limit, signal to noise (S/N) value, and desorption time can be significantly improved by photo illumination, thus providing a plausible way to design high performance gas sensors based on 2D materials with nanoscale defects.

## Method

The detailed experiments and characterizations are shown in the ESI.†

## Author contributions

H. C. W. conceived the study. D. Y. C., and Y. L. L. grew the sample. W. J. Y., H. J. X. and Z. W. fabricated the sample. J. C., M. C., and B. S. C. carried out the TEM measurements. W. J. Y. and C. C. performed the gas sensing measurements. H. R. F. and C. R. C. conducted the DFT simulation. Z. T. J. and H. J. L. gave scientific advice. H. C. W., W. J. Y., D. Y. C., and C. C. wrote the manuscript. All authors discussed the results and commented on the manuscript.

## Conflicts of interest

There no conflicts to declare.

## Acknowledgements

This work was supported by the National Key R&D Program of China (Grant No. 2017YFE0301404 and 2017YFA0303800), the National Natural Science Foundation of China (No. 61874010, 11804237), and by the Science and Technology Innovation Program for Creative Talents in Beijing Institute of Technology (No. 2017CX01006).

## References

- 1 B. Liu, L. Chen, G. Liu, A. N. Abbas, M. Fathi and C. Zhou, *ACS Nano*, 2014, 8(5), 5304–5314.
- 2 A. N. Abbas, B. Liu, L. Chen, Y. Ma, S. Cong, N. Aroonyadet, M. Köpf, T. Nilges and C. Zhou, *ACS Nano*, 2015, 9(5), 5618–5624.



- 3 S. S. Shendage, V. L. Patil, S. A. Vanalakar, S. P. Patil, N. S. Harale, J. L. Bhosale, J. H. Kim and P. S. Patil, *Sens. Actuators, B*, 2017, **240**, 426–433.
- 4 T. Xu, Y. Pei, Y. Liu, D. Wu, Z. Shi, J. Xu, Y. Tian and X. Li, *J. Alloys Compd.*, 2017, **725**, 253–259.
- 5 C. Hao, P. B. Shepson, J. W. Drummond and K. Muthuramu, *Anal. Chem.*, 1994, **66**(21), 3737–3743.
- 6 <https://www.epa.gov/criteria-air-pollutants/naaqs-table>.
- 7 J. Kong, N. R. Franklin, C. Zhou, M. G. Chapline, S. Peng, K. Cho and H. Dai, *Science*, 2000, **287**(5453), 622–625.
- 8 E. Rossinyol, A. Prim, E. Pellicer, J. Arbiol, F. Hernández-Ramírez, F. Peiró, A. Cornet, J. R. Morante, L. A. Solovyov, B. Tian, T. Bo and D. Zhao, *Adv. Funct. Mater.*, 2007, **17**(11), 1801–1806.
- 9 F. Schedin, A. K. Geim, S. V. Morozov, E. W. Hill, P. Blake, M. I. Katsnelson and K. S. Novoselov, *Nat. Mater.*, 2007, **6**(9), 652–655.
- 10 J. D. Fowler, M. J. Allen, V. C. Tung, Y. Yang, R. B. Kaner and B. H. Weiller, *ACS Nano*, 2009, **3**(2), 301–306.
- 11 S. Deng, V. Tjoa, H. M. Fan, H. R. Tan, D. C. Sayle, M. Olivo, S. Mhaisalkar, J. Wei and C. H. Sow, *J. Am. Chem. Soc.*, 2012, **134**(10), 4905–4917.
- 12 F. K. Butt, C. Cao, W. S. Khan, Z. Ali, R. Ahmed, F. Idrees, I. Aslam, M. Tanveer, J. Li and S. Zaman, *Mater. Chem. Phys.*, 2012, **137**(137), 565.
- 13 F. K. Perkins, A. L. Friedman, E. Cobas, P. M. Campbell, G. G. Jernigan and B. T. Jonker, *Nano Lett.*, 2013, **13**(2), 668–673.
- 14 W. Yuan, A. Liu, L. Huang, C. Li and G. Shi, *Adv. Mater.*, 2013, **25**(5), 766–771.
- 15 N. Huo, S. Yang, Z. Wei, S.-S. Li, J.-B. Xia and J. Li, *Sci. Rep.*, 2014, **4**, 5209.
- 16 H. Long, A. Harley-Trochimczyk, T. Pham, Z. Tang, T. Shi, A. Zettl, C. Carraro, M. A. Worsley and R. Maboudian, *Adv. Funct. Mater.*, 2016, **26**(28), 5158–5165.
- 17 J. Zhang, X. Liu, G. Neri and N. Pinna, *Adv. Mater.*, 2016, **28**(5), 795–831.
- 18 J. Baek, D. Yin, N. Liu, I. Omkaram, C. Jung, H. Im, S. Hong, S. M. Kim, Y. K. Hong, J. Hur, Y. Yoon and S. Kim, *Nano Res.*, 2017, **10**(8), 2904.
- 19 Z. Feng, Y. Xie, E. Wu, Y. Yu, S. Zheng, R. Zhang, X. Chen, C. Sun, H. Zhang, W. Pang, J. Liu and D. Zhang, *Micromachines*, 2017, **8**(5), 155.
- 20 B. Cho, J. Yoon, S. K. Lim, A. R. Kim, D.-H. Kim, S.-G. Park, J.-D. Kwon, Y.-J. Lee, K.-H. Lee, B. H. Lee, H. C. Ko and M. G. Hahm, *ACS Appl. Mater. Interfaces*, 2015, **7**(30), 16775–16780.
- 21 L. Kou, T. Frauenheim and C. Chen, *J. Phys. Chem. Lett.*, 2014, **5**(15), 2675–2681.
- 22 S. Weidong, H. Lihua, W. Haishui, Z. Hongjie, Y. Jianhui and W. Pinghui, *Nanotechnology*, 2006, **17**(12), 2918.
- 23 D. J. Late, T. Doneux and M. Bougouma, *Appl. Phys. Lett.*, 2014, **105**(23), 233103.
- 24 J. Z. Ou, W. Ge, B. Carey, T. Daeneke, A. Rotbart, W. Shan, Y. Wang, Z. Fu, A. F. Chrimes, W. Wlodarski, S. P. Russo, Y. X. Li and K. Kalantar-zadeh, *ACS Nano*, 2015, **9**(10), 10313–10323.
- 25 Y. Li, S. G. Leonardi, A. Bonavita, G. Neri and W. Wlodarski, *Procedia Eng.*, 2016, **168**, 1102–1105.
- 26 W. Yang, L. Gan, H. Li and T. Zhai, *Inorg. Chem. Front.*, 2016, **3**(4), 433–451.
- 27 Y. Huang, E. Sutter, J. T. Sadowski, M. Cotlet, O. L. A. Monti, D. A. Racke, M. R. Neupane, D. Wickramaratne, R. K. Lake, B. A. Parkinson and P. Sutter, *ACS Nano*, 2014, **8**(10), 10743–10755.
- 28 G. Su, V. G. Hadjiev, P. E. Loya, J. Zhang, S. Lei, S. Maharjan, P. Dong, P. M. Ajayan, J. Lou and H. Peng, *Nano Lett.*, 2015, **15**(1), 506–513.
- 29 J. Xia, D. Zhu, L. Wang, B. Huang, X. Huang and X.-M. Meng, *Adv. Funct. Mater.*, 2015, **25**(27), 4255–4261.
- 30 X. Zhou, Q. Zhang, L. Gan, H. Li and T. Zhai, *Adv. Funct. Mater.*, 2016, **26**(24), 4405–4413.
- 31 J. Hao, D. Zhang, Q. Sun, S. Zheng, J. Sun and Y. Wang, *Nanoscale*, 2018, **10**(15), 7210–7217.
- 32 D. Gu, X. Li, Y. Zhao and J. Wang, *Sens. Actuators, B*, 2017, **244**, 67–76.
- 33 R. Li, K. Jiang, S. Chen, Z. Lou, T. Huang, D. Chen and G. Shen, *RSC Adv.*, 2017, **7**(83), 52503–52509.
- 34 K. Xu, N. Li, D. Zeng, S. Tian, S. Zhang, D. Hu and C. Xie, *ACS Appl. Mater. Interfaces*, 2015, **7**(21), 11359.
- 35 H. Chen, Y. Chen, H. Zhang, D. W. Zhang, P. Zhou and J. Huang, *Adv. Funct. Mater.*, 2018, **28**(20), 1801035.
- 36 M. Ma, H. Khan, W. Shan, Y. Wang, J. Z. Ou, Z. Liu, K. Kalantar-zadeh and Y. Li, *Sens. Actuators, B*, 2017, **239**, 711–717.
- 37 Y. Xiong, W. Xu, D. Ding, W. Lu, L. Zhu, Z. Zhu, Y. Wang and Q. Xue, *J. Hazard. Mater.*, 2018, **341**, 159–167.
- 38 Z. Qin, K. Xu, H. Yue, H. Wang, J. Zhang, C. Ouyang, C. Xie and D. Zeng, *Sens. Actuators, B*, 2018, **262**, 771–779.
- 39 C. Kim, J. C. Park, S. Y. Choi, Y. Kim, S. Y. Seo, T. E. Park, S. H. Kwon, B. Cho and J. H. Ahn, *Small*, 2018, **17**04116.
- 40 M. Ma, H. Khan, W. Shan, Y. Wang, J. Z. Ou, Z. Liu, K. Kalantar-zadeh and Y. Li, *Sens. Actuators, B*, 2017, **239**, 711–717.
- 41 D. Gu, X. Li, Y. Zhao and J. Wang, *Sens. Actuators, B*, 2017, **244**, 67–76.
- 42 Z. Yang, H. Liang, X. Wang, X. Ma, T. Zhang, Y. Yang, L. Xie, D. Chen, Y. Long and J. Chen, *ACS Nano*, 2015, **10**(1), 755–762.
- 43 B. Cho, M. G. Hahm, M. Choi, J. Yoon, A. R. Kim, Y.-J. Lee, S.-G. Park, J.-D. Kwon, C. S. Kim, M. Song, Y. Jeong, K.-S. Nam, S. Lee, T. J. Yoo, C. G. Kang, B. H. Lee, H. C. Ko, P. M. Ajayan and D.-H. Kim, *Sci. Rep.*, 2015, **5**, 8052.
- 44 D. Barreca, D. Bekermann, E. Comini, A. Devi, R. A. Fischer, A. Gasparotto, C. Maccato, G. Sberveglieri and E. Tondello, *Sens. Actuators, B*, 2010, **149**(1), 1–7.
- 45 J. Deng, Z. Luo, X. Wu and Y. Hu, *Min. Sci. Technol.*, 2010, **20**(4), 557–562.
- 46 Z. S. Hosseini, A. I. zad and A. Mortezaali, *Sens. Actuators, B*, 2015, **207**, 865–871.
- 47 Y. Gong, H. Yuan, C.-L. Wu, P. Tang, S.-Z. Yang, A. Yang, G. Li, B. Liu, J. van de Groep, M. L. Brongersma, M. F. Chisholm, S.-C. Zhang, W. Zhou and Y. Cui, *Nat. Nanotechnol.*, 2018, **13**(4), 294–299.



- 48 J. Shen, G. Liu, K. Huang, Z. Chu, W. Jin and N. Xu, *ACS Nano*, 2016, **10**(3), 3398–3409.
- 49 G. Chen, T. M. Paronyan, E. M. Pigos and A. R. Harutyunyan, *Sci. Rep.*, 2012, **2**, 343.
- 50 S. Park, S. An, H. Ko, S. Lee and C. Lee, *Sens. Actuators, B*, 2013, **188**, 1270–1276.
- 51 S. Park, S. An, Y. Mun and C. Lee, *ACS Appl. Mater. Interfaces*, 2013, **5**(10), 4285–4292.
- 52 J. H. Ahn, M. J. Lee, H. Heo, H. S. Ji, K. Kim, H. Hwang and M. H. Jo, *Nano Lett.*, 2015, **15**(6), 3703.
- 53 L. A. Currie, Quellenangabe, *Pure Appl. Chem.*, 1995, 1699–1723.
- 54 J. Li, Y. Lu, Q. Ye, M. Cinke, J. Han and M. Meyyappan, *Nano Lett.*, 2003, **3**(7), 929–933.
- 55 K. Lee, R. Gatensby, N. McEvoy, T. Hallam and G. S. Duesberg, *Adv. Mater.*, 2013, **25**(46), 6699–6702.
- 56 Y. Wu, D. Zhang, K. Lee, G. S. Duesberg, A. Syrlybekov, X. Liu, M. Abid, M. Abid, Y. Liu and L. Zhang, *Adv. Mater. Technol.*, 2016, 1600197.
- 57 P. E. Blöchl, *Phys. Rev. B: Condens. Matter Mater. Phys.*, 1994, **50**(24), 17953–17979.
- 58 C. Wen, Q. Ye, S.-L. Zhang and D. Wu, *Sens. Actuators, B*, 2016, **223**, 791–798.
- 59 M. Zhu, X. Li, S. Chung, L. Zhao, X. Li, X. Zang, K. Wang, J. Wei, M. Zhong, K. Zhou, D. Xie and H. Zhu, *Carbon*, 2015, **84**, 138–145.
- 60 H.-Y. Kim, K. Lee, N. McEvoy, C. Yim and G. S. Duesberg, *Nano Lett.*, 2013, **13**(5), 2182–2188.
- 61 J. P. Burrows, A. Dehn, B. Deters, S. Himmelmann, A. Richter, S. Voigt and J. Orphal, *J. Quant. Spectrosc. Radiat. Transfer*, 1998, **60**(6), 1025–1031.

